university of groningen

faculty of mathematics and natural sciences

kapteyn astronomical institute

Probing the kinematic structure of massive cores with molecular lines

John J. Dolan
Kapteyn Astronomical Institute
University of Groningen
Supervisor: Russell F. Shipman

June 24, 2016

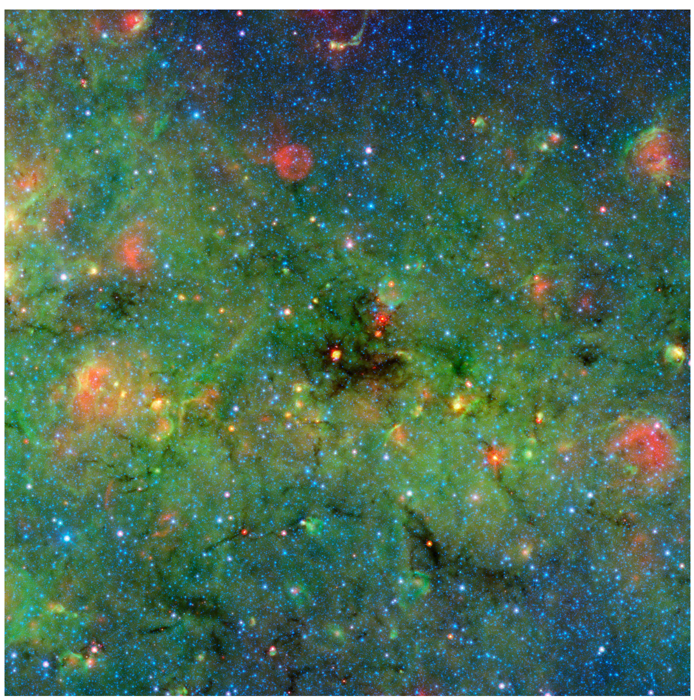

Abstract

Context: The earliest stages of high mass star formation are not very well understood. "Infrared Dark Clouds" (IRDCs) are a promising candidate for the potential birthplaces of massive stars. By observing molecular lines in these clouds, we can build a picture of the chemical and dynamical structure of the embedded cores in these clouds and study the early stages of high mass star formation.

Aim: The goal of this project is to investigate the kinematic structure of high mass envelopes to further our understanding of the processes involved.

Method: Using the 1D radiative transfer code, RATRAN, I aim to make use of the observations of two sub-mm bright clumps (Shipman et al., 2014) of N_2H^+ (6-5)and (3-2)transitions, as well as a $C^{17}O$ (3-2)transition.

Results: From the analysis of the observed lines it was found that both G28-MM and G11-MM show signs of infalling material with velocities ranging from 0.1kms^{-1} to 2.8kms^{-1}. The turbulent velocities in these cores were found to range from 0.6kms^{-1} to 2.0kms^{-1} and increasing from the center. Abundances of N_2H^+ were estimated to be on the order of 1x10^{-9} and $C^{17}O$ abundances of 1x10^{-6}. These parameters were then probed further to build a picture of the kinematic structure of the envelopes surrounding these cores.

Conclusion: A kinematic step function was required as no individual model fits all line together. The kinematic and molecular structures found for both cores in this project are consistent with previous observations and studies.

Contents

1 Introduction

1.1 Background

Stars begin their lives when a cloud of interstellar gas and dust begins to collapse under it's own self-gravity. When gravitational forces overcome outward pressures, collapse begins. Material flows from lower to higher density regions. These dense regions become more compact and begin to heat up, forming a hot protostellar core. The protostars at the center of the cores are surrounded by an envelope and can accrete material for $\sim 3x10^5$yr (Behrend and Maeder, 2001) . Probing this envelope can improve our understanding of the initial conditions of low and high mass star formation.

How do massive stars form?
One of the greatest outstanding questions in this era of Astronomy is high mass star formation (HMSF). High mass stars are defined as stellar objects larger than $>10M_\odot$. The issue with understanding how these objects form is three-fold. The first problem is their rarity and distance from Earth. For every 1000 Solar mass stars, there is only a single $10M_\odot$ star (Stolte, 2013). The nearest $>10M_\odot$ main sequence star to us (in the Trapezium cluster) is 400pc away, making the task of obtaining spatially resolved objects difficult. Several review articles address some of these issues further Zinnecker and Yorke (2007); Beuther et al. (2007).

Another issue with observing the formation of massive stars is their rapid evolution. Massive stars are born, join the main sequence and die in a supernova explosion within 10^6 years (Soderblom et al., 2014). This makes it extremely rare to catch one in a particular phase of evolution. This is the main reason for the mystery surrounding HMSF.

A third hindrance in our attempt to understand the formation of these objects is their location. As these stars form in cold, dense clouds, they are often deeply obscured by thick dust clouds, making visible wavelength observations impossible. Since high mass cores and their envelopes cannot be observed at visble-MIR wavelengths, they appear bright at sub-mm wavelengths. Therefore it is useful to observe many rotational molecular lines to probe the complex processes and structures of the envelopes surrounding these objects. It is for this reason FIR - sub-mm range space based telescopes like Herschel (HIFI) and ground based telescope like APEX are essential tools in our arsenal to tackle this mystery.

Why study IRDCs?
Infrared dark clouds appear as dark patches or silhouettes across the sky in visible and even infrared wavelengths, hence "infrared dark". They are seen in absorption against mid-IR background emission. These clouds exhibit a filamentary structure made of gas and dust, and can be several thousand times the mass of the Sun. Since their discovery in the mid-90's, IRDCs have been widely theorised to be potential birthplaces of massive, $>10M_{\odot}$ stars (Carey et al., 1998b) but have also shown low mass star formation (van der Wiel and Shipman, 2008).

IRDCs are very cold structures, typically <20K (Egan et al., 1998). This combination of low temperature and high density allows for complex chemistry to take place. Using sub-mm and far-IR space/ground based telescopes, we can examine the complex chemistry of these clouds by observing molecular line emission/absorption and build a picture of the physical conditions and complex processes taking place in the objects at the very earliest stages of evolution.

What can we learn?
Photometric analysis of these sub-mm bright object can tell us what stage of evolution the high mass star is at. Observing continuum (dust) emission can offer clues of whether the surrounding envelopes are quiescent or active (ie. jets). Photometry data can also constrain the mass of the source(s) and the dust in the protostellar envelope.

Spectroscopic analysis of these regions involves observing molecular line emission/absorption. Different molecules may also require vastly contrasting physical conditions to survive at a steady state abundance, hence certain molecules can be sensitive to certain conditions. For example, SiO emission is often used as a probe for shocks caused by supersonic jets emanating from the protostellar object (due to sputtering of dust grains) (Leurini et al., 2014). While CS can be used as a dense gas tracer (Helfer and Blitz, 1997). Chemical evolutionary processes allow us to set constraints on the age and phase of evolution of star forming cores. Observations of molecular lines can provide a wealth of information regarding the ages and physical conditions like masers, outflows, jets, and accretion rates.

1.2 Line formation

Radiative transfer is the emission/absorption of light by matter. The energy of a photon from a radiation source will be absorbed by a molecule, atom or dust particle and be re-emitted in a random direction in the form of a secondary photon at a wavelength corresponding to the rotational/vibrational energy of the molecule. This secondary photon may then be absorbed again by other molecules, and emitted again until the photons can escape the cloud. Depending on the motion of the gas in the cloud and the molecular lines observed, it is possible to determine the dynamics and the abundance of such a molecule using radiative transfer codes like RATRAN.

The abundance of a given molecule can be determined by the flux of the line produced. The intensity of the line is indicative of the abundance or column density of the molecule, ie. a larger abundance will show a stronger line (for optically thin lines).. The turbulent velocity (Brownian motion) can be estimated from the width of the line, ie. the larger the turbulence the wider the line. An asymmetry in the line profile/shape can indicate contraction/expansion or rotation of the cloud.

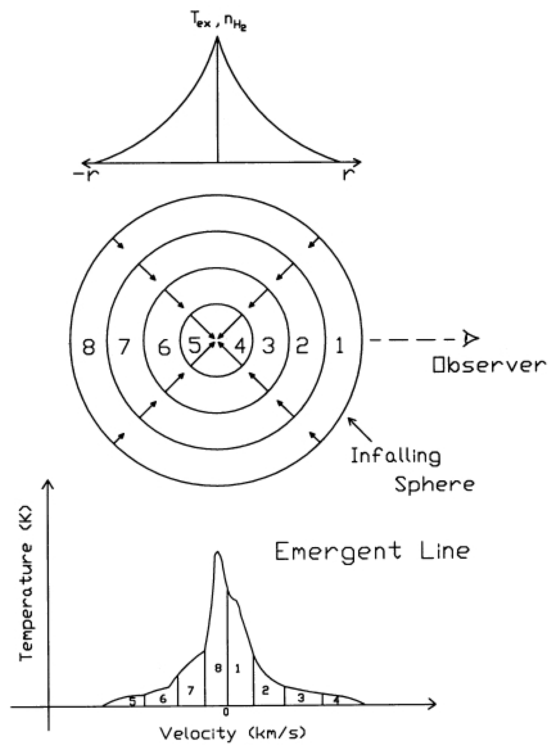

Figure 1.1: Classic infall signature a line (Walker et al., 1994). Top panel: Temperature/density vs radius. Middle panel: Gas motion of the envelope. Bottom panel: Resulting line shape reflecting the motion and structure of the envelope.

For infalling gas, a blue shifted line is observed. This is shown in Figure 1.1, where the back-side of the cloud produces a stronger peak (to the left) due to the fact that it suffers less extinction effects than the receding, redshifted near-side (w.r.t the observer). This makes the overall line profile asymmetric in shape. The opposite is true for outflowing gas, where the line is redshifted (line profile shifts to lower frequencies). Rotation can also cause asymmetries in the line, which gives rise to both red and blue asymmetric lines.

Optically thin lines show defined peaks, whereas optically thick lines show some level of self absorption. Self absorption (optically thick lines) can indicate the opacity of a given line. This occurs when photons being emitted from a molecule are absorbed by neighbouring molecules and scattered in all directions, not necessarily in the direction of the observer. A line is said to be self absorbed if it's optical depth is larger than 1 (Gary, 2012).

2 Method

2.1 RATRAN

RATRAN (Hogerheijde and van der Tak, 2000) is a 1D accelerated Monte Carlo radiative transfer code. RATRAN allows for the analysis of gas dynamics and abundances from observed sub-mm lines. It has two main components, AMC and SKY. AMC reads a molecular file containing information on the molecule to be modelled. This file, obtained from the LAMDA database (Leiden Atomic and Molecular Database), contains the Einstein A coefficients, upper energy levels, collision rates, cross-sections and multiple transitions for a given molecule (Schöier et al., 2005). AMC can assume a plane-parallel or spherically symmetric distribution of dust and gas (spherically symmetric distribution was chosen for this project). Based on the temperature and density profiles, AMC calculates the population of energy states of the molecule within each radial bin. Sky performs the radiative transfer to produce a spectral map near the frequency of the molecular line transition. A third party program, GREG (Grenoble Graphic), is then used to plot the view the modelled line profile. The RASM code (Chavarria, 2015) was used to link these steps together. The temperature and density profile were created using multi-wavelength photometric measurements of the dust continuum emission (Chavarria, 2015). The temperature and density profiles for G28-MM and G11-MM are shown in Figure 2.1, showing the temperature and density increasing toward the center.

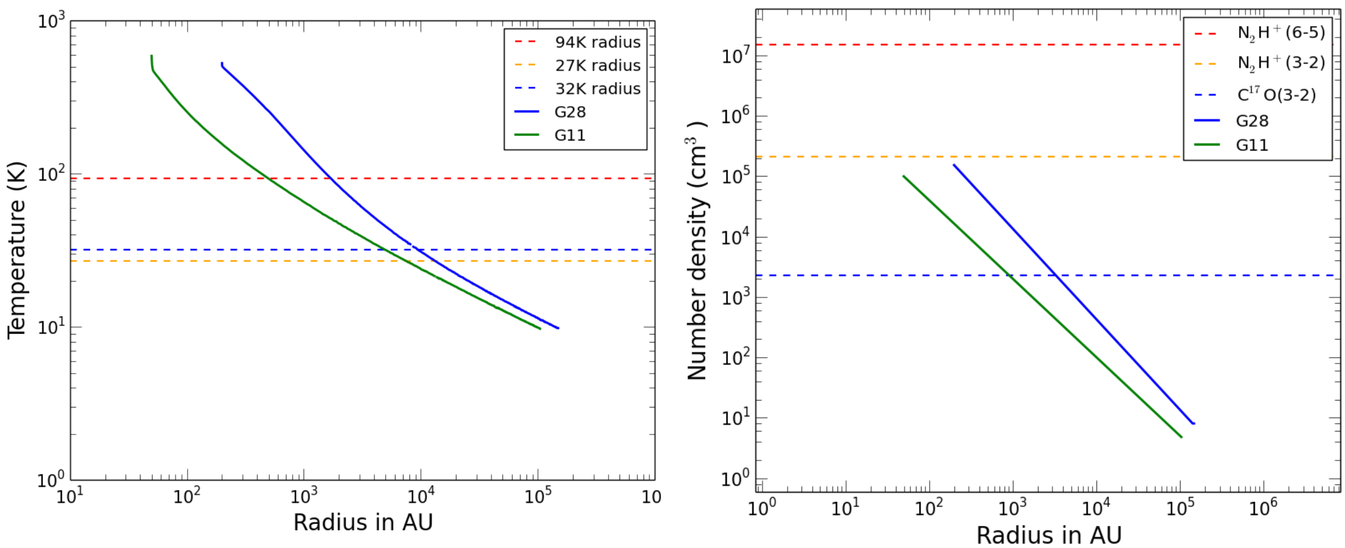

Figure 2.1: Dust temperature and gas density profiles for G28-MM and G11-MM. Temperature profile shows excitation temperatures of the molecules (and transition levels). Density profile show critical densities of the molecules (and transition levels). Red: N_2H^+ (6-5), Orange:N_2H^+ (3-2), Blue: $C^{17}O$ (3-2).

2.1.1 Approach

RATRAN allows the user to vary the inner/outer abundance, infall/outflow velocity and the turbulent velocity of the model. By varying these parameters and computing the best fit model parameters I hope to form a single kinematic model, consistent with the observed lines from each core.

2.2 Observations

The observational data used in this project were carried out by as part of the Water in Star forming regions with Herschel program (WISH) with Herschel's HIFI instrument and with Atacama Experiment telescope (APEX) (Shipman et al., 2014). The two clumps in IRDCs G28.34+0.06 and G11.11-0.12 were observed at sub-mm wavelengths and have corresponding spectral and photometric data. APEX observed N_2H^+ at the (3-2)transition (279.5 GHz) and Herschel HIFI observed the N_2H^+ (6-5)line (558.96 GHz). APEX also observed the $C^{17}O$ (3-2) line at 337.8 GHz. The beam sizes for Herschel HIFI and APEX were 38" and 22" respectively. The HIFI data has a typical noise of ∼7mK while APEX data has noise values ranging from 250-750mK.

Core Properties							
ID	Long name	Position	v_{LSR} (kms^{-1})	T_{kin} (K)	$N(H^{+}H_2)$ ($10^{22}cm^{-2}$)	Distance (kpc)	Mass ($M_\odot$)
G28-MM	G28.34+0.06 P2	RA: 18:42:52.40 DEC: -3:59:54.0	78.5	16.0	32.7	4.8	2310
G11-MM	G11.11-0.12 P2	RA: 18:10:28.40 DEC: -19:22:29.0	29.2	13.8	10.2	3.6	172

Table 2.1: Shipman et al. (2014)

Table 2.1 shows the properties of each core such as v_{LSR} (systemic velocity), gas temperature (T_{kin}), total column density ($N(H^{+}H_2)$), distance and core mass. The masses and column densities of these core were based on dust continuum emission while the gas temperature, kinematic distance and v_{LSR} were obtained from NH_3 observations (Carey et al., 1998a; Pillai et al., 2006).

Observed line Properties							
Species	Frequency (GHz)	E_u (K)	HPBW (")	Observatory	T_{sys} (K)	δv (kms^{-1})	n_{crit}[1] (cm^{-3})
N_2H^+(6-5)	558.96666	93.9	38	HIFI 1A	76	0.6	1.5e7
N_2H^+(3-2)	279.511701	26.8	22	APEX	120-210	0.53	2.07e5
$C^{17}O$ (3-2)	337.061129	32.4	18	APEX	130	0.87	2.3e3

Table 2.2: Shipman et al. (2014),
(1) calculated from LAMBDA database file.

Table2.2 shows the upper energy level (E_u), the Half Power Beamwidth (HPBW), the telescope/instrument used in observations, the total system temperature, the channel width and the critical density of the molecule at the given energy level. n_{crit} was calculated using the Einstein A coefficient (A_{ul}) and the sum of the collision rates (K_{ui}) at temperatures ranging from 10K-2000K (n_{crit}=$A_{ul}/\sum K_{ui}$).

The lines to be modelled are shown in Figure 2.2:

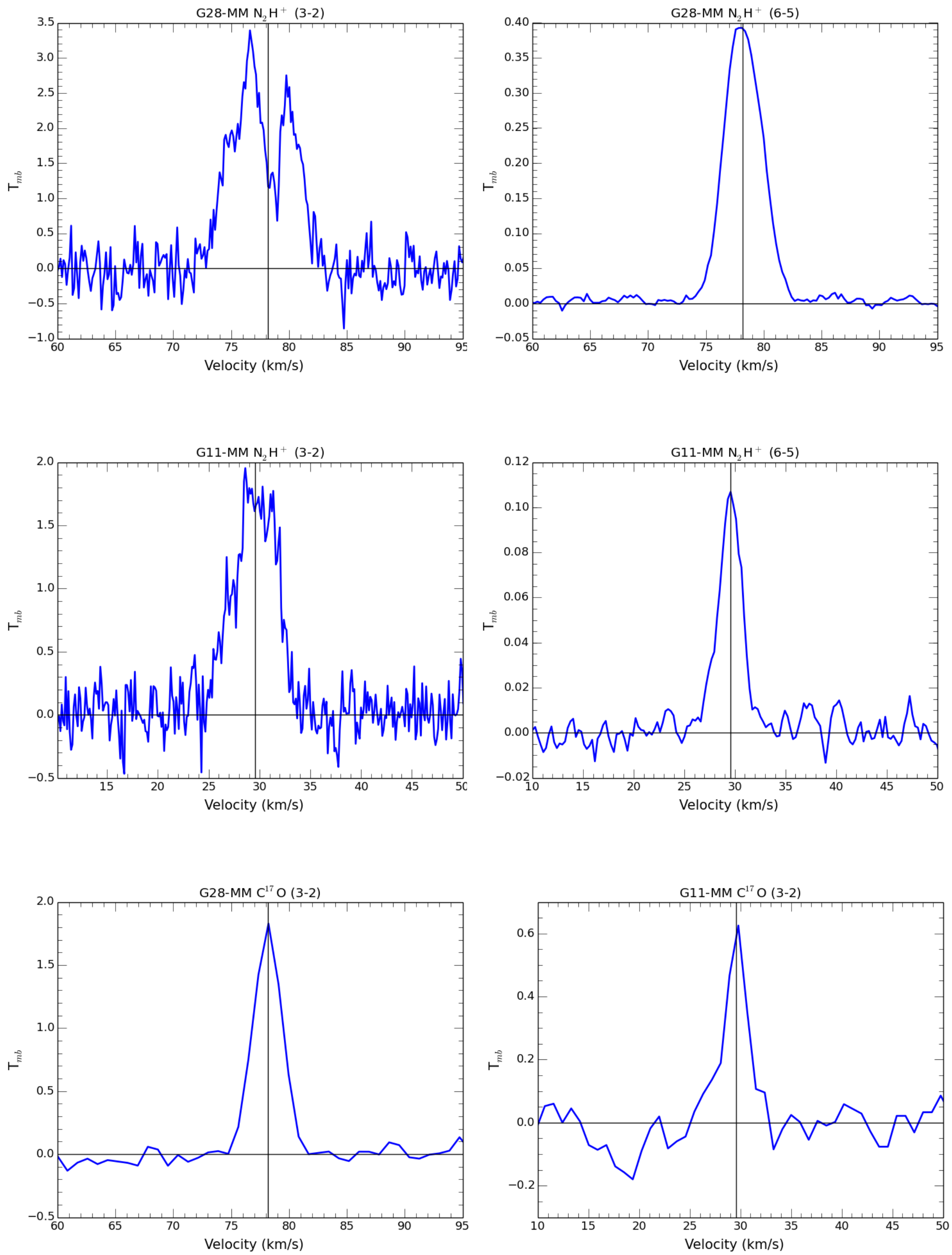

Figure 2.2: Observed lines with their respective V_{lsr} and continuum subtracted level plotted in black

2.3 $\chi_\nu{}^2$ Minimization

I initially used a reduced $\chi_\nu{}^2$ analysis to find the best fitting parameters for these observations. The reduced $\chi_\nu{}^2$ is defined in Eq. 2.2.

$$\chi^2 = \sum_i \frac{(Data_i - Model_i)^2}{\sigma_i^2} \tag{2.1}$$

$$\chi_v^2 = \frac{\chi^2}{\nu} \tag{2.2}$$

where i is the frequency, ν is the number of free parameters and σ is the rms of the data.

The chi-square minimization technique (Bevington and Robinson, 2002) is implemented to find the best fitting parameters and to constrain the limits on those parameters. In this analysis only two parameters were varied while the rest kept constant. The aim of this practice is to find the lowest lying $\chi_\nu{}^2$ in $\chi_\nu{}^2$ parameter space corresponding to the best fitting values. This was done for each line to find the best turbulent velocity, inner and outer abundance and infall/expansion velocity. The $\chi_\nu{}^2$ is estimated channel-by-channel, comparing the y-position of the data vs the y-position of the model.

Once the best fitting models were chosen, the value of each of the parameters were varied once again until the χ^2 increased by 1 from the minimum to provide a 1σ error value for each parameter (Bevington and Robinson, 2002).

3 Results

3.1 $\chi_\nu{}^2$ Minimization

3.1.1 G28-MM N_2H^+ (3-2)

In Figures 3.1 - 3.6, the results for the G28 (3-2) line models are shown.

In Figure 3.1, the turbulent velocity was set to vary with constant abundance (equal inner and outer abundance). The range of values were chosen between two extremes, from a constant abundance that showed no line emission to an abundance were the line showed significantly larger intensity than the observed line. The turbulent velocity was also varied between two extremes, where the line was too narrow to too wide. The contours are set at 1σ, 2σ, 3σ from the minimum, ie the minimum $\chi_\nu{}^2$ of the distribution increases by factor 2 within the 1σ contours, by a factor 3 in 2σ contours and by a factor 4 in the 3σ contours. The lowest corresponding $\chi_\nu{}^2$ model is shown in figure 3.2.

Figure 3.3 shows the inner vs outer abundance test. This test was run with the turbulent velocity set to the lowest $\chi_\nu{}^2$ model value from the previous test (1.8kms^{-1}). The inner and outer abundance's were again chosen to extreme ranges. It is clear from this plot that the inner region is not being probed by these models. This will be discussed in greater detail in the discussion section. The best model in this test is shown in figure 3.4.

Figure 3.5 shows the infall/expansion tests where the outer abundance alone was varied with infall/expansion velocity. The infall/expansion values were chosen based on visual inspection of the line prior to tests. There is clear sign of infall in this line, so only a small range of expansion velocity (positive radial velocity) was chosen. It is also obvious from the $\chi_\nu{}^2$ distribution that there is no definitive result using this technique. Figure 3.6 shows the best model according to the $\chi_\nu{}^2$ distribution test. Clearly, the model is not the best fit and further testing was required.

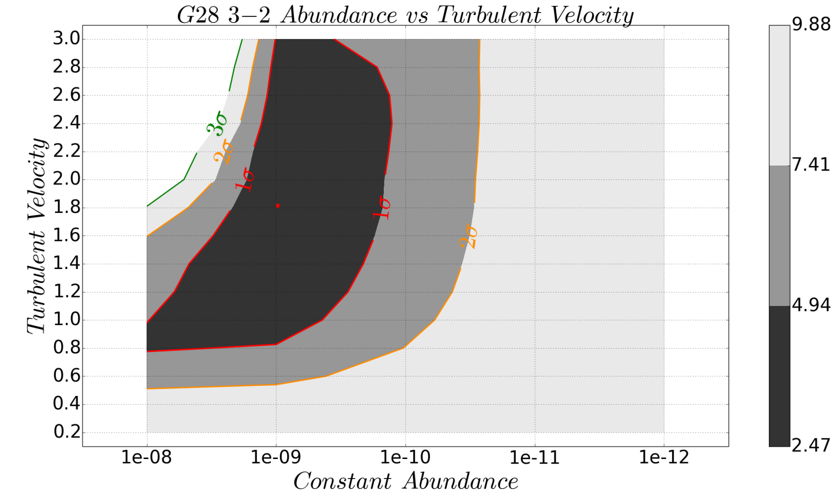

Figure 3.1: $\chi_\nu{}^2$ distribution:
V_{turb} vs Constant abundance

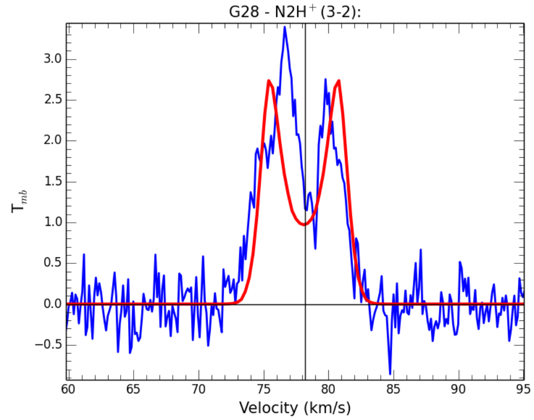

Figure 3.2: V_{turb}=1.8kms^{-1}
Abundance=1e-9

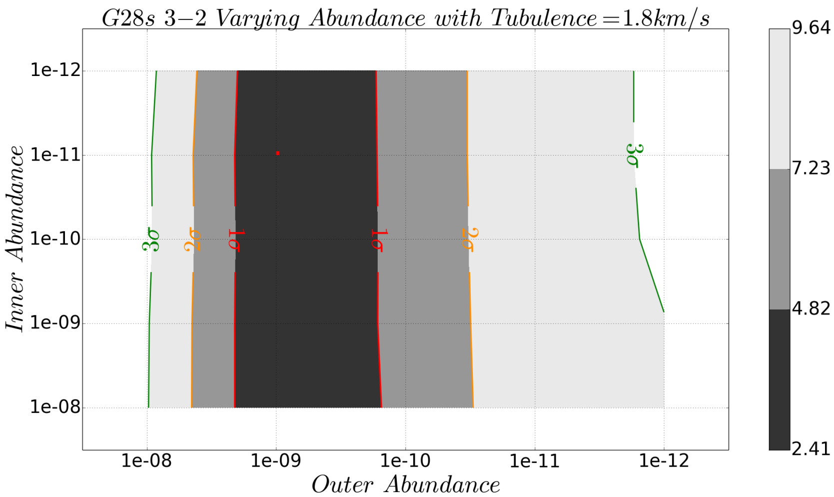

Figure 3.3: $\chi_\nu{}^2$ distribution:
Inner vs Outer abundance

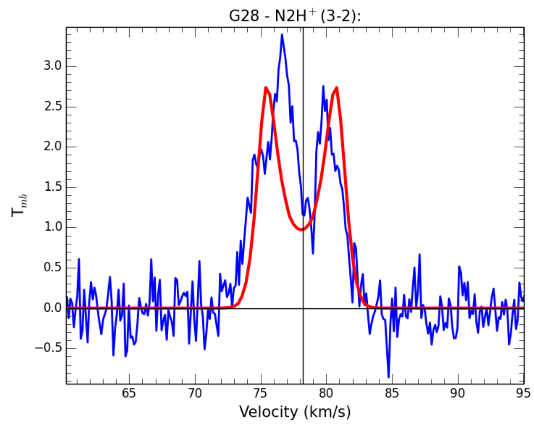

Figure 3.4: V_{turb}=1.8kms^{-1}
Outer abundance=1e-9
Inner abundance = 1e-11

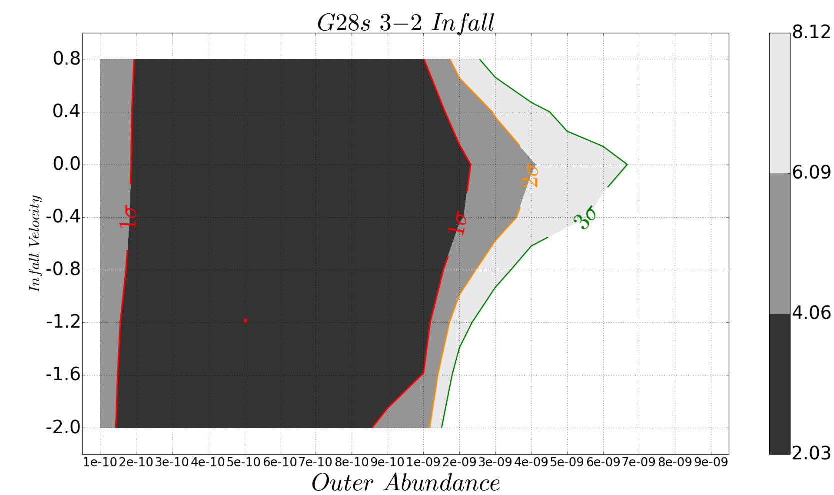

Figure 3.5: $\chi_\nu{}^2$ distribution:
Expansion/Infall Velocity vs Outer abundance

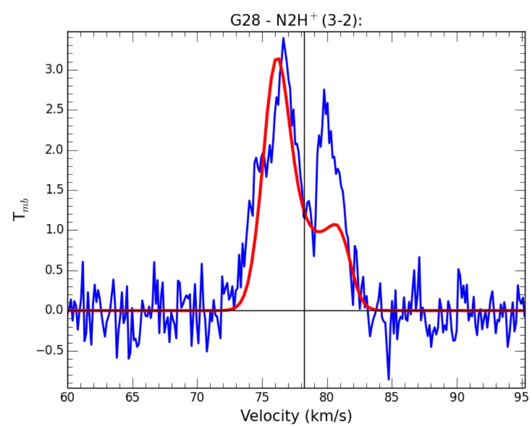

Figure 3.6: V_{turb}=1.8kms^{-1}
Outer abundance=1e-9
Inner abundance = 1e-11
Infall= 1.2kms^{-1}

In the Figures 3.1 - 3.6, it is evident that the ${\chi_\nu}^2$ minimization technique is not sufficient for reproducing models which are consistent with the observed line. Further analysis was required. This required visual analysis, where models were run individually and examined for their line shape and similarity to the observed lines. This test proved to be much more efficient and more effective than the ${\chi_\nu}^2$ minimization approach. The visual inspection method also allowed for exponent testing, whereby the parameter can be set to vary with radius. The N_2H^+ (3-2) and (6-5) lines probe different radii from the source, allowing us to test the properties of different regions of the envelopes.

These ${\chi_\nu}^2$ minimization tests were performed on all lines but were found to be unreliable in identifying viable parameters. Therefore, the ${\chi_\nu}^2$ is used as a guide while χ^2 is used as a gauge for errors in the parameters.

3.2 G28-MM analysis

3.2.1 Result - Infall

In this section I aim to show why infall is necessary to create a consistent model, not only in terms of the asymmetry of the line, but also the intensity. It is assumed that the intensity of an optically thin line represents the abundance, whereby a large abundance is seen in a higher intensity line than a lower abundance.

In Figure 3.7, we see the comparison between models for G28-MM N_2H^+ (6-5) with no infall and an infall with a velocity of 2.7kms^{-1}. It is clear that the model in Figure 3.7(a) lacks the intensity and width in the observed line while also showing signs of self absorption, not seen in the data. Figure 3.7(b) shows a model with infall velocity sufficient to accurately reproduce the observed line. Not only does the addition of infall increase the intensity of the line, it also shows a broader component which is consistent with the width of the observed line.

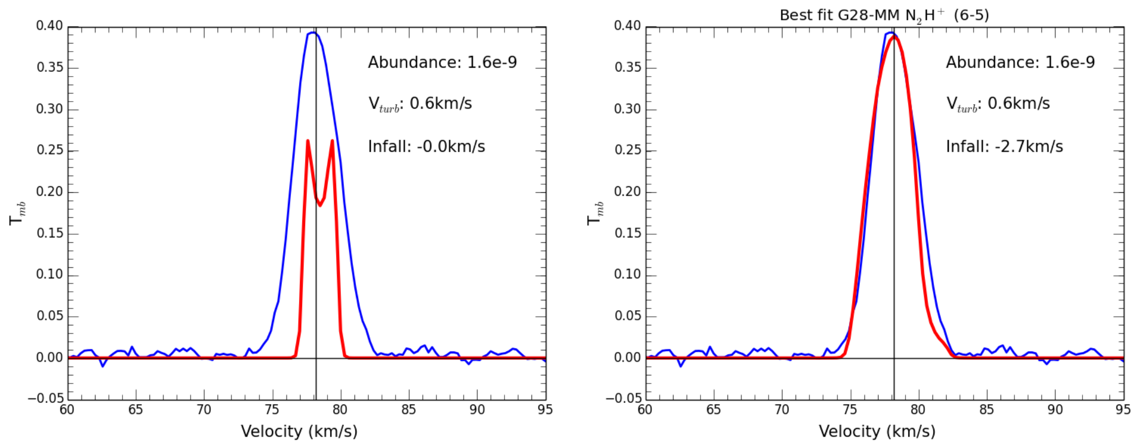

(a) (b)

Figure 3.7: (a) No infall. Outer abundance: 1.6e-9, V_{turb}: 0.6kms^{-1}, Infall: 0.0 kms^{-1}.
(b) Best fit model. Outer abundance: 1.6e-9, V_{turb}: 0.6kms^{-1}, Infall: 2.7kms^{-1}.

The parameters that produce the model of best fit for the N_2H^+ (6-5) line are shown in the caption in Figure 3.7(b).

3.2.2 Consistency check

As described in Section 3.2.1, the requirement for infall is essential in obtaining a consistent model for the N_2H^+ (6-5) line in G28-MM. Although the upper energy levels of the N_2H^+ (6-5) (94K) and (3-2) (27K) are different, it is possible that the kinematics of both lines could be the same. If we now assume that the physical and dynamical conditions probed in the N_2H^+ (6-5) line are the same as the N_2H^+ (3-2) line, we would expect the parameters for the (3-2) to be consistent with the best fitting (6-5) line parameters.

Here we introduce the same parameters for the N_2H^+(6-5) line into the (3-2) line model. The result can be seen in Figure 3.8.

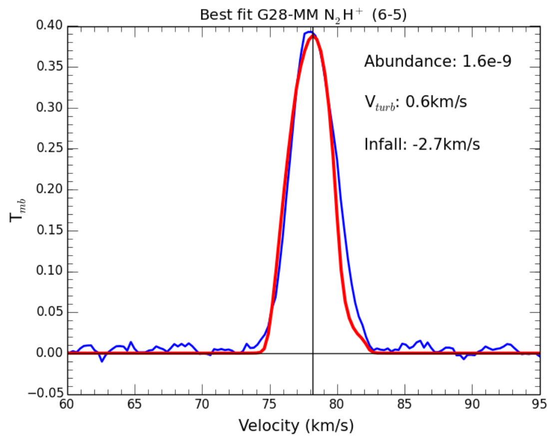

(a)

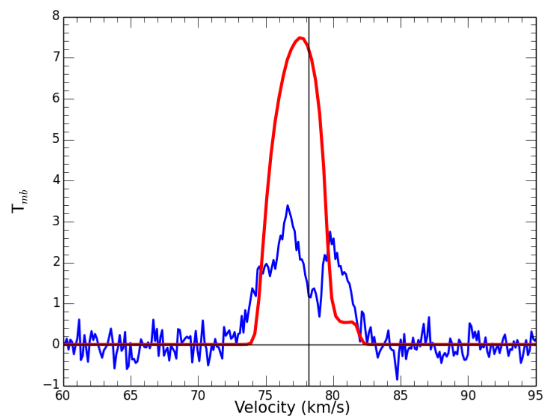

(b)

Figure 3.8: (a) Best fit N_2H^+ (6-5) model.
(b) N_2H^+ (3-2) model with best fitting (6-5) parameters

Figure 3.8 shows that the dynamics probed with N_2H^+ (6-5) model are inconsistent with the dynamics in the N_2H^+ (3-2) line. This result points to a difference in both models that cannot be reproduced with a single kinematic parameter.

3.2.3 Result - Turbulence

The results for the G28-MM N_2H^+ (3-2) showed inconsistencies in the results for the turbulent velocity. While testing the turbulence in the N_2H^+ (3-2) line model, it is evident that no single turbulent velocity model has the ability to form both peaks and wings consistent with those seen in the observed line. It is for this reason that I show in Figure 3.9 that the N_2H^+ (3-2) shows two separate turbulent velocity components.

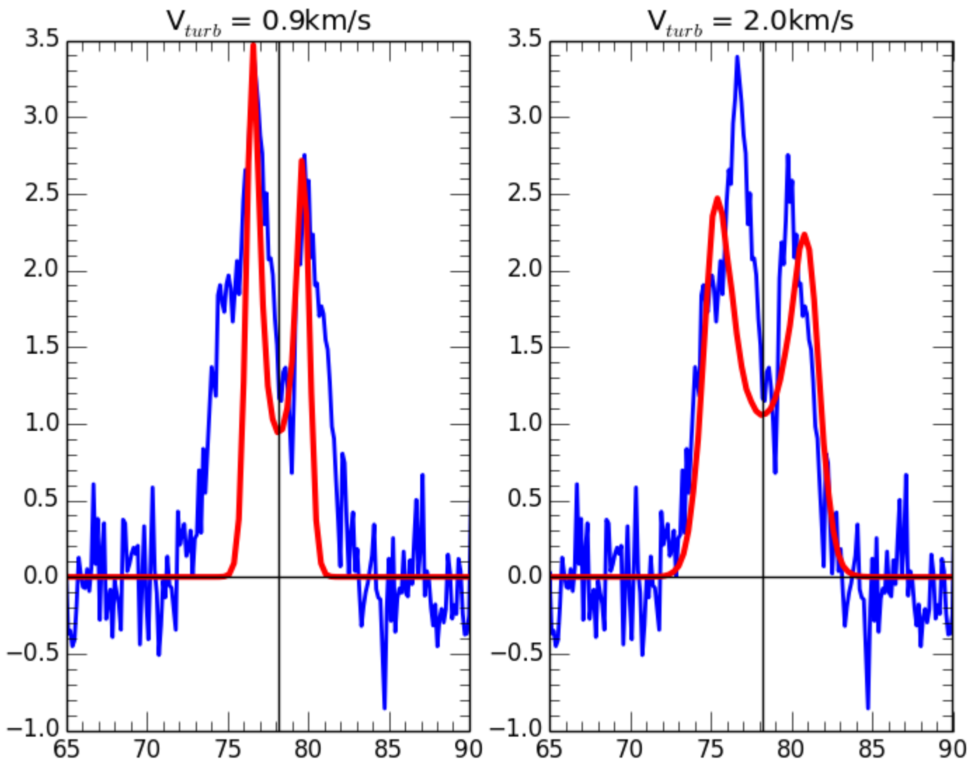

Figure 3.9: G28-MM (3-2)line shows a consistent fit for peaks with a turbulence of 0.9kms^{-1} and a consistent fit for the wings at 2.0kms^{-1} turbulence. Outer abundance = 8e-10

As we can see in Figure 3.9, the narrow (0.9km/s) component forms a model consistent with the observed line peaks, while the broad (2.0km/s) component fits the wings. Clearly no single turbulent velocity can replicate the observed line peaks and wings simultaneously. The narrow turbulent velocity component does allow for the estimation on the infall velocity, however, as the asymmetry in the peaks is an indication of infall.

To probe this finding further an exponent was implemented, whereby the turbulent velocity was set to vary with radius. The result of this turbulence exponent is seen in Figure 3.10.

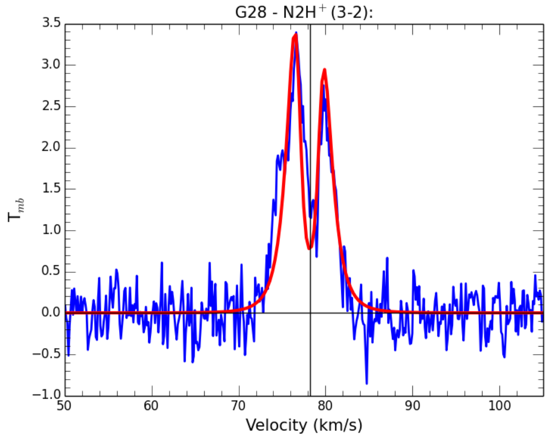

(a)
Outer abundance:8e-10,
V_{turb}(initial) 0.7kms^{-1},
Infall: 0.1kms^{-1},
V_{turb} exponent: -0.5

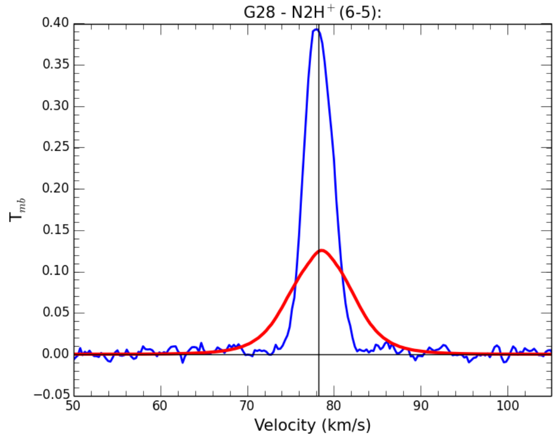

(b)
Outer abundance:8e-10,
V_{turb}(initial) 0.7kms^{-1},
Infall: 0.1kms^{-1},
V_{turb} exponent: -0.5

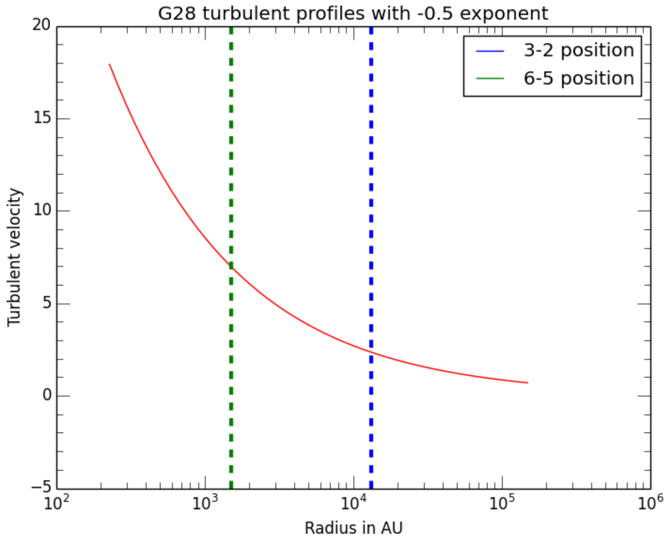

(c)
Turbulence profile with -0.5 exponent. 94K and 27K radius in dashed lines corresponding to the upper energy levels of the N_2H^+ (6-5) and (3-2) respectively.

Figure 3.10

In Figures 3.10a-c, we see that although the turbulence exponent model provides a consistent fit for the N_2H^+ (3-2) line, the same model fails to reproduce a consistent line width for the N_2H^+ (6-5) line.

Note: An Infall velocity exponent was also introduced and also produced models inconsistent with the data. This can be seen in Appendix B.

3.2.4 Consistency check

We see from Section 3.2.3 that a turbulent exponent model does not adequately reproduce models consistent with both the N_2H^+ (3-2) and (6-5) line. However, using the results found in Section 3.2.3 (ie. the broad turbulent velocity required to fit the wings and the infall velocity obtained from the narrow turbulence model), we can make an individual best fitting model for the N_2H^+ (3-2) and test these parameter against the N_2H^+ (6-5) model. The results are shown in Figure 3.11.

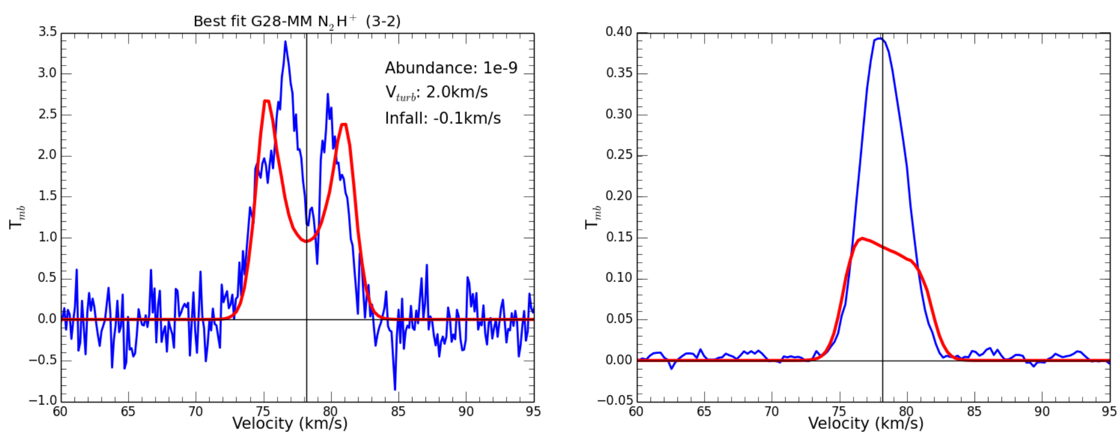

(a) (b)

Figure 3.11:
(a)Best fit N_2H^+ (3-2) model.
(b)N_2H^+ (6-5) line with best fitting (3-2) parameters

Once again, Figure 3.11 shows an incompatibility between the N_2H^+ (3-2) and (6-5) model parameters. These finding point to a requirement for two individual models, one with kinematic parameters consistent with the N_2H^+ (3-2) line and the other with N_2H^+ (6-5) line.

3.2.5 Result - G28-MM C^{17}O

Figure 3.12 shows the model with the best fitting parameters for the C^{17}O line in G28-MM.

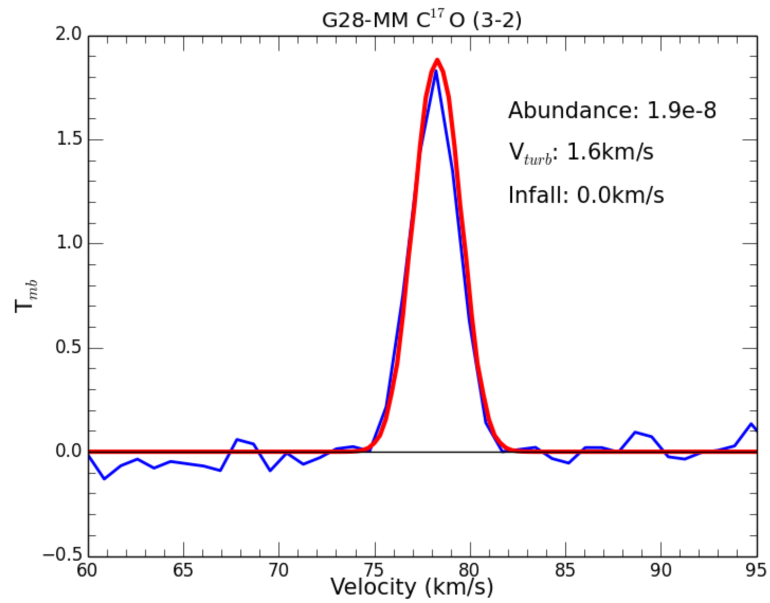

Best fit model for C^{17}O (3-2) in G28-MM

Figure 3.12

The parameters in the model shown in Figure 3.12 produce a synthetic line profile that is consistent with the observed data.

3.2.6 Result - Creating a Single Kinematic Structure Model

Now that we have all the best fitting parameters for the G28-MM molecular lines, we need to build a single dynamical model that is consistent with all the observed lines. It is evident from the results described in Section 3.2.3 (and in 5) that an exponent in the turbulence or infall velocity does not produce models that are consistent with the data. Therefore, a simpler step function was created. This step function would contain jumps of turbulence and infall velocities at the appropriate radius in the model. These radii were estimated by changing the infall or turbulent velocity in each grid bin until a single kinematic model was created which produced models consitent with all observed lines. For example, the N_2H^+(6-5) line shows an infall velocity of 2.7km/s. Starting with the inner most radial bin in the model (N_2H^+(6-5) has an upper energy level of 96K and should probe the inner/warmer regions), I changed the infall velocity bin-by-bin from 0km/s to 2.7km/s until a consistent N_2H^+ (6-5) model was produced, giving a estimate to which radii the (6-5) line is probing.

Taking all the dynamical parameters from each line, a single kinematic model was created that was consisted with all observed lines. This result is shown in Figure 3.13.

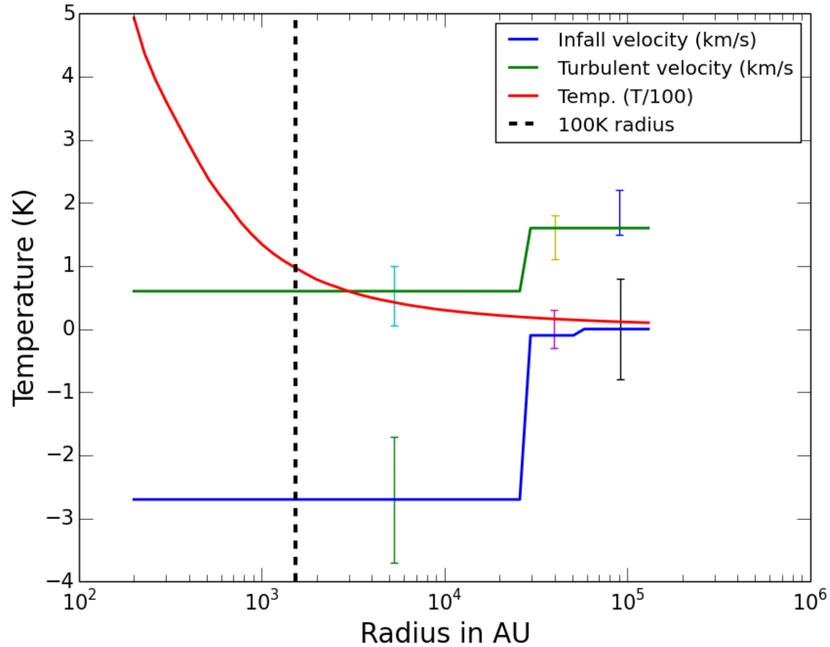

(a)

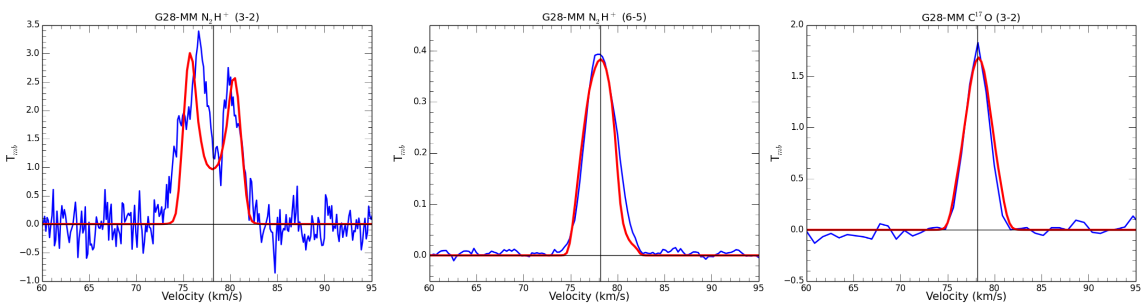

(b) (c) (d)

Figure 3.13: (a) Kinematic stepfunction for G28-MM. (b) N_2H^+(3-2) model line profile produced. (c)N_2H^+(6-5) model line profile produced. (d) $C^{17}O$ (3-2)model line profile produced. Abundance is set to 1.0x10^{-9} for the N_2H^+ (3-2) and 1.6x10^{-9} for N_2H^+ (6-5). The N_2H^+ (3-2)line corresponds to a turbulent velocity of 1.6kms^{-1} and infall of 0.1kms^{-1}. The N_2H^+ (6-5)line shows a turbulence of 0.6kms^{-1} and 2.7kms^{-1} infall. $C^{17}O$ (3-2)line shows a turbulence of 1.6kms^{-1} and no infall

Figure 3.13 shows that a single kinematic structure can be introduced that produces modelled line profiles that are consistent with the observed data for G28-MM.

3.3 G11-MM analysis

The steps taken in the G11-MM analysis followed the procedure outlined in Section 3.2.

As with the G28-MM analysis on N_2H^+, the best fitting parameters for both lines were found and then inserted into the the other corresponding model. In Figure 3.14, the best fitting N_2H^+ (6-5) parameters are modelled in the N_2H^+ (3-2) line.

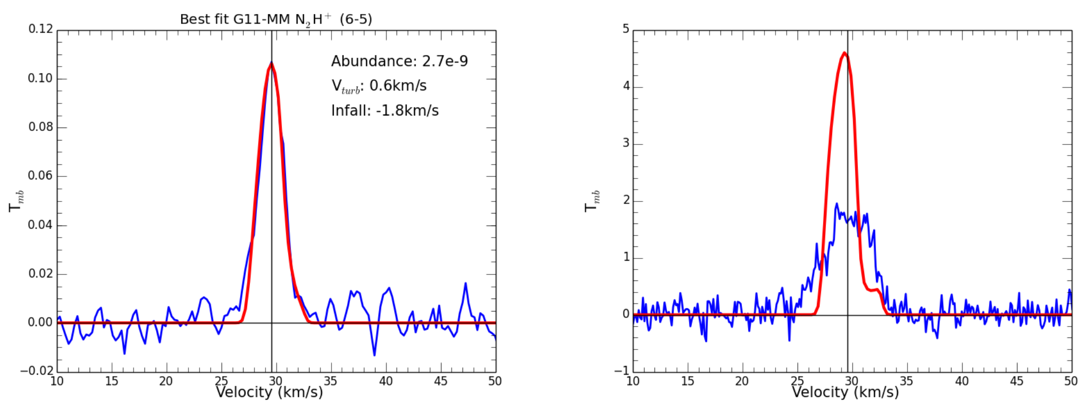

(a)
Outer abundance: 2.7e-9,
V_{turb}: 0.6kms^{-1},
Infall: 1.8kms^{-1}

(b)
Outer abundance: 2.7e-9,
V_{turb}: 0.6kms^{-1},
Infall: 1.8kms^{-1}

Figure 3.14

Clearly, as with G28-MM, the parameters in the G11-MM N_2H^+ (6-5) is not consistent with the N_2H^+ (3-2) line. The best fitting N_2H^+ (6-5) parameters overestimate the level of intensity seen in the (3-2) line while failing to accurately fit the wings of the line.

Finding the best fitting parameters for the G11-MM N_2H^+ (3-2) line proved difficult as the shape of the line could not be fit to any degree of accuracy. However, by exploiting the slope of the asymmetry in the peak of the line, it was possible to obtain and estimate on the infall velocity. Tests were run with varying outer abundances in order to show the minimum abundance at which self absorption appears to strongly influence the modelled line and to reproduce the line shape with a less intense model. The results are shown in Figure 3.15.

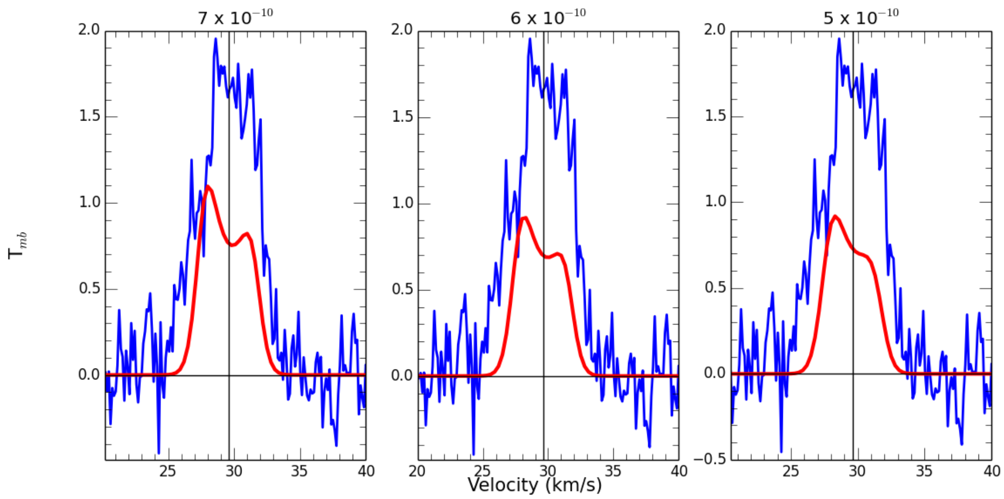

Figure 3.15: Outer abundance: 7e-10, 6e-10 and 5e-10, V_{turb}: 1.5kms^{-1}, Infall: -0.4kms^{-1}

In Figure 3.15 we see that with an outer abundance of 7e-10, the model over predicts the level of self absorption seen in the observed line, increasing the outer abundance will result in a deeper self absorption feature in the model. However the slope of the line peak in the model is consistent with the slope of the observed line peak, indicating an infall velocity of ~0.4km/s.

Since it was not possible to accurately obtain an outer abundance fitting for this line, it is assumed that the abundance found for the (3-2)line is equal to that of (6-5)line, 2.7x10^{-9}. The best fitting parameter model for the N_2H^+ (3-2)in G11-MM is shown in Figure 3.16a. Again, we test the best fitting N_2H^+ (3-2) model paramters against the N_2H^+ (6-5) model. This is shown in Figure 3.16b.

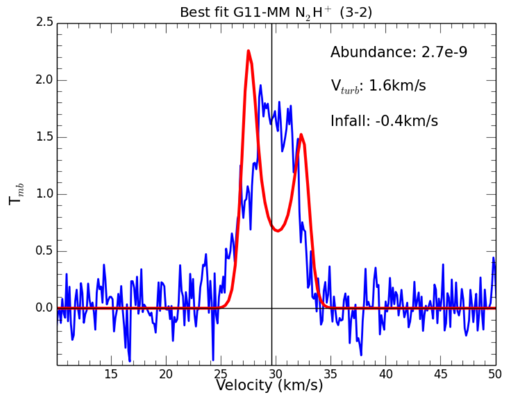

(a)
Outer abundance: 2.7e-9, V_{turb}: $1.6kms^{-1}$, Infall: $0.4kms^{-1}$

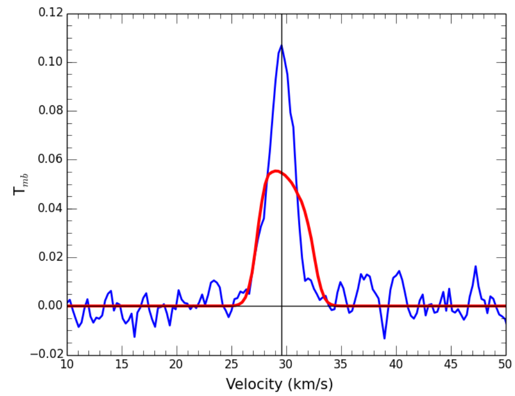

(b)
Outer abundance: 2.7e-9, V_{turb}: $1.6kms^{-1}$, Infall: $0.4kms^{-1}$

Figure 3.16

Once again, no single kinematic parameter is consistent with both G11-MM N_2H^+ lines together. The best fitting parameters for the $C^{17}O$ (3-2) line in G11-MM are shown in Figure 3.17, showing similar abundance and dynamics to the G28-MM $C^{17}O$ (3-2) line. As with described in Section 3.2 (G28-MM analysis), a single kinematic step function was required to reproduce all the observed lines in G11-MM. This result is shown in Figure 3.18.

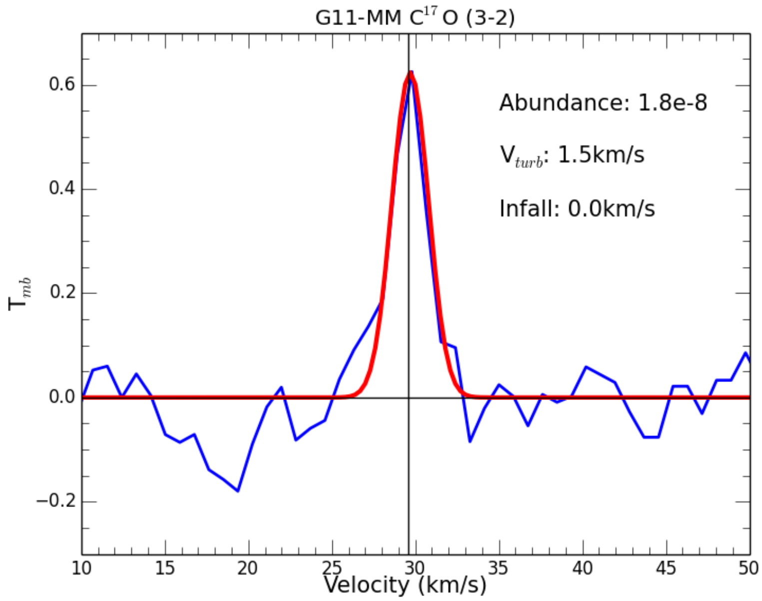

Best fit model for $C^{17}O$ (3-2) in G11-MM

Figure 3.17

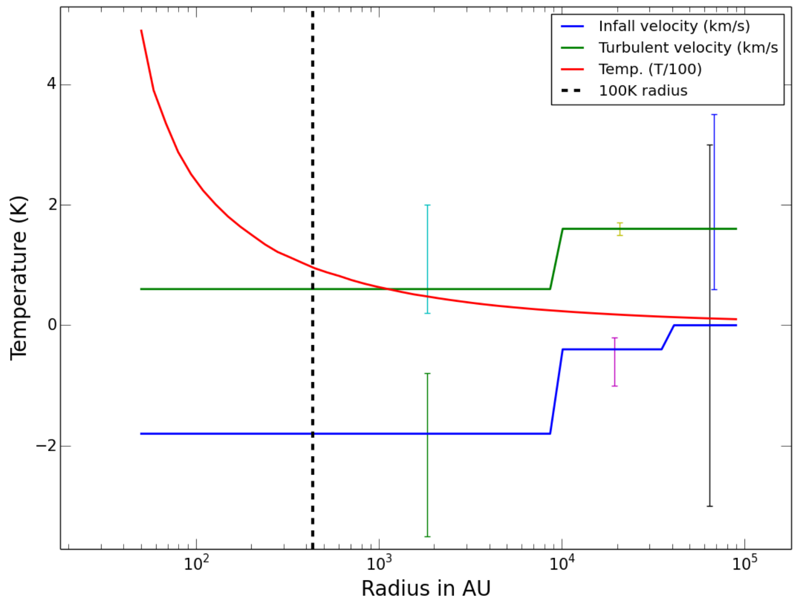

(a)

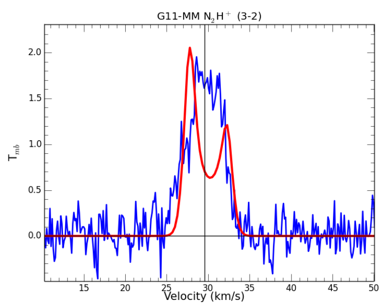

(b)

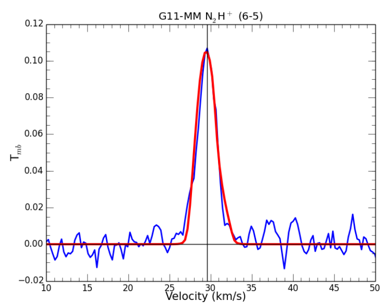

(c)

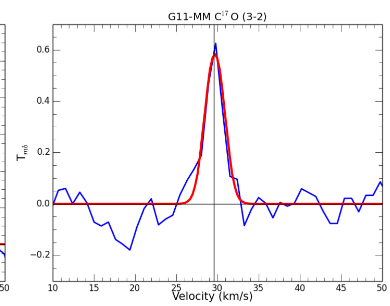

(d)

Figure 3.18: (a) Kinematic step function for G11-MM. (b) N_2H^+(3-2) model line profile produced. (c) N_2H^+(6-5) model line profile produced. (d) $C^{17}O$ (3-2)model line profile produced. Abundance is set to 2.7x10^{-9} for the N_2H^+ (3-2) and for N_2H^+ (6-5) models. The N_2H^+ (3-2)line corresponds to a turbulent velocity of 1.6kms^{-1} and infall of 0.4kms^{-1}. The N_2H^+ (6-5)line shows a turbulence of 0.6kms^{-1} and 1.8kms^{-1} infall. $C^{17}O$ (3-2)line shows a turbulence of 1.6kms^{-1} and no infall

Figure 3.18 shows that a single kinematic structure can be introduced that produces modelled line profiles that are consistent with the observed data for G11-MM.

3.4 Final Parameters

Once all the optimum models were obtained, we can now add the errors to these estimates. By increasing the χ^2 found in the best fitting models by 1, we then have a 1σ deviation. By varying each parameter (outer abundance, turbulence and infall velocity) until the model shows a χ^2 equivalent to a 1σ deviation, this will define the error limits on the parameters found. Because the models for the optically thin lines are a better fit to the date, the resulting chi-square was low ($\sim$1). The optically thick model fits are not as accurate as the optically thin lines and therefore have a higher best fit χ^2 ($\sim$90). Therefore an increase in χ^2 from 1 - 2 will show a larger error range than χ^2 90 - 91. It is for this reason the errors in the optically thin lines are greater (in general) than the optically thick lines.

Final best fit parameters (N_2H^+):				
Core	Molecular transition	Abundance (e-9)	Turbulence (kms^{-1})	Infall Velocity (kms^{-1})
G28-MM	N_2H^+ (3-2)	$1^{+0.2}_{-0.1}$	$2.0^{+0.2}_{-0.5}$	$0.1^{+0.4}_{-0.2}$
G28-MM	N_2H^+ (6-5)	$1.6^{+1.5}_{-1}$	$0.6^{+0.4}_{-0.55}$	$2.7^{+1.0}_{-1.0}$
G11-MM	N_2H^+ (3-2)	$*2.7^{+2.3}_{-2.3}$	$1.6^{+0.1}_{-0.1}$	$0.4^{+0.2}_{-0.6}$
G11-MM	N_2H^+ (6-5)	$2.7^{+2.3}_{-2.3}$	$0.6^{+1.4}_{-0.4}$	$1.8^{+1.7}_{-1.0}$

Table 3.1:
* abundance assumed to be equal to that found for G11-MM N_2H^+ (6-5)

Final best fit parameters ($C^{17}O$):				
Core	Molecular transition	Abundance (e-8)	Turbulence (kms^{-1})	Infall Velocity (kms^{-1})
G28-MM	$C^{17}O$ (3-2)	$1.9^{+0.6}_{-1.3}$	$1.6^{+0.1}_{-0.6}$	$0.0^{+0.8}_{-0.8}$
G11-MM	$C^{17}O$ (3-2)	$1.8^{+1.7}_{-1.2}$	$1.5^{+2.0}_{-0.9}$	$0.0^{+3.0}_{-3.0}$

Table 3.2

4 Discussion

4.1 Comparing Final Parameters to Results in the Literature

4.1.1 Abundance/Column density

The abundances of N_2H^+ ($\sim$1x10^{-9}) found in both cores in this study are very consistent with other findings, where estimates N_2H^+ abundances of several (high mass and low mass) sources are found to be on the order of 10^{-9} (Olmi et al., 2015; Miettinen and Offner, 2013).

To estimate the column densities, I used the H+H_2 column density of 32.7x10^{22}cm^{-2} for G28-MM and 10.7x10^{22}cm^{-2} for G11-MM (Shipman et al., 2014). This leads to an estimate of N_2H^+ column density of $\sim$3x10^{14}cm^{-2} ($\sim$1x10^{-9} x 32.7x10^{22}cm^{-2}) for G28-MM. Previous observations of G28-MM N_2H^+ (3-2) line emission estimates a column densities of $\sim$1x10^{13}cm^{-2}, an order of magnitude less (Chen et al., 2010). Given the different techniques used (calculations through excitation temperature and radiative transfer), this is consistent.

Studies of $C^{17}O$ in circumstellar material around high mass protostars concluded that the $C^{17}O$ abundances ranged from 6e-9 to 1e-7 from column density estimates using line intensities Thomas and Fuller (2008). These values are consistent with the abundance of $\sim$1.9x10^{-8} for $C^{17}O$ found in this project. Observations of the IRDC G304.74+01.32 have also shown $C^{17}O$ abundances of $\sim$9x10^{-8} (Miettinen, 2012), within an order of magnitude deviation from the result in this project.

4.1.2 Turbulence/Line width

N_2H^+ (3-2)line Δv for G28-MM has been estimated to show a FWHM of 6.14kms^{-1}, corresponding to a σ of $\sim$2.6kms^{-1}, well within the margin of error found for the (3-2)line in this study.(Chen et al., 2010)

Estimates of N_2H^+ (6-5) line widths (FWHM) range from a σ of $\sim$0.8kms^{-1} to 2.0kms^{-1}, quite larger than the 0.6kms^{-1} found in this study. These findings are based on Gaussian fits and not radiative transfer models (Olmi et al., 2015; Miettinen and Offner, 2013).

Previous observations (Herpin et al., 2016; Larson, 1981; Herpin et al., 2012; San José-García et al., 2016) and models (McKee and Tan, 2003) have shown that turbulence increases with radius from the center in high and low mass protostellar envelopes.

The results in this study support these previous results, showing that the turbulence is larger in the outer regions than the inner regions.

4.1.3 Infall

Observations of the HCO^+ (1-0) line in G28-MM estimate an infall velocity of $0.84kms^{-1}$ (Feng et al., 2016), consistent with the infall velocities obtained in this project, although this molecule at this energy level may be probing a different part of the envelope.

4.1.4 Gas Density

Estimates of gas density have been proposed previously for these cores (Shipman et al., 2014). From this project, the N_2H^+ column density in G28-MM is estimated to be $\sim 3x10^{14}$. This corresponds to a gas number density of $\sim 10^6$. The $C^{17}O$ abundance ($1.9x10^{-8}$) gives a column density of $\sim 6x10^{15}cm^{-2}$, giving a gas density between $\sim 10^5$ and $\sim 10^6$ cm^{-3}.

The models of G11-MM N_2H^+ abundance gives a column density of $2.8x10^{14}cm^{-2}$ ($2.7x10^{-9}$ x $10.7x10^{22}cm^{-2}$), again, corresponding to a gas number density of $\sim 10^6cm^{-2}$. The column density of $C^{17}O$ ($2x10^{15}cm^{-2}$), giving a gas density of $\sim 10^6cm^{-3}$.

The analysis of N_2H^+ (3-2) and (6-5) lines have shown that although the abundances agree, the turbulent velocities and infall velocities do not. Since the N_2H^+ (3-2) transition has a lower excitation temperature (27K) than the (6-5) (94K), it is assumed that the corresponding lines must be formed within different regions of the envelope. The (3-2)line probes an outer component of the envelope while the (6-5)probes the inner envelope. This gives us the ability to build a kinematic structure profile.

It is evident that the conditions in the (6-5)region and (3-2)region are quite different. Most notable is the infall velocity, which shows that there is considerably less asymmetry in the (3-2)line than the (6-5)infall velocity predicts. This could imply an infall velocity profile or an inward acceleration perhaps. Clearly the assumption that conditions are the same is not supported by the data.

4.2 Theoretical Infall

We have seen that the infall velocities have a large influence on the line shape and intensity. To test if the infall velocity values obtained are similar to the expected theoretical infall velocities (based on the mass of the core and distance from the center) we used Eq. 4.1 to compute the theoretical infall velocities and compare them to the values obtained in this project.

$$V_{inf} = \left(\frac{GM}{R}\right)^{1/2} \tag{4.1}$$

(Stahler and Palla, 2004)

where G is the gravitational constant, M is the source mass and R is the radius from the source.

G28-MM contains two massive compact cores with masses of $47M_{\odot}$ and $97\mathrm{M}_{\odot}$ (Zhang et al., 2009). From the temperature profile, the excitation temperature of N_2H^+ (3-2) (27K at 17000AU) and N_2H^+ (6-5) (94K at 1500 AU) gives an approximation of the radius at which these emission lines are expected to trace. Using Equation 4.1, the (3-2)line should show an infall velocity of around 2.7kms^{-1} and the (6-5)line is expected to show approximately 9.2kms^{-1} infall. These values are significantly larger than what is found in the RATRAN models. To test this, the values obtained were implemented into the corresponding models. The result from this test can be seen in Figure 4.1.

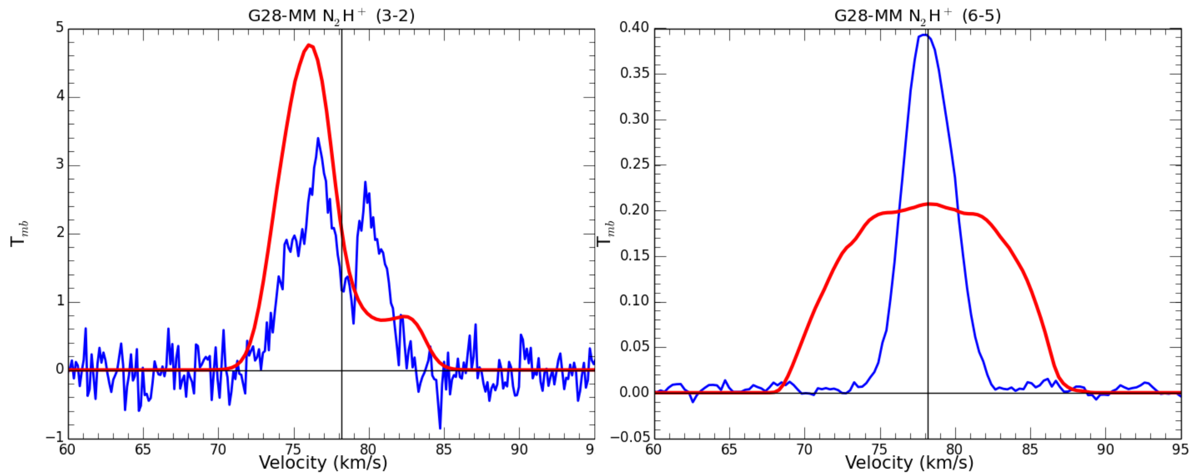

N_2H^+ (3-2) with 2.4kms^{-1} infall N_2H^+ (6-5) with 9.2kms^{-1} infall

Figure 4.1: Theoretical infall velocities implemented into the N_2H^+ (3-2) and N_2H^+ (6-5) lines

It is clear that the theoretical values do not produce models that are consistent with the observed lines as they over-estimate the intensity and widths of the lines. It is not clear why the N_2H^+ (6-5) shows such a broad model.

4.3 Insignificance of the Inner abundance

The inner abundance proved insignificant in all of these models. This was seen in the chi-square distribution in Figure 3.3 but can be seen more clearly in Figure 4.2 (N_2H^+) and Figure 4.3 ($C^{17}O$). We suspected that beam dilution was the probable cause for this as the inner region is defined at >100K region (defined by the temperature jump) corresponds to a radius 1/240th the radius of the G11-MM model and 1/96th of the G28-MM model, giving an area 10^5 times smaller than the total model area. Therefore, even with a large inner abundance, the emission from this region would not significantly effect the line produced. To test this, the beam size was reduced by 10^5 and, again, the inner abundance was set to vary 4 orders of magnitude. This would "force" the inner region to show some emission. The models for this test are shown in Figure 4.4.

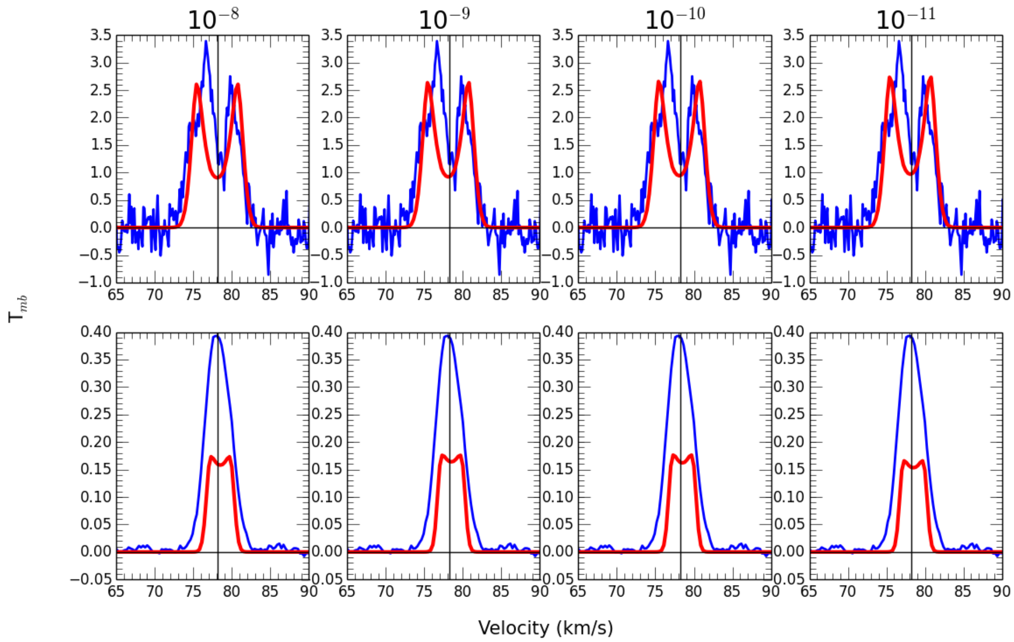

Figure 4.2: Models with a range of inner abundances for (3-2)and (6-5)line with all other parameters kept constant
(3-2)line parameters: Outer abundance: 1e-9, V_{turb}=1.8kms^{-1}, no infall
(6-5)line parameters: Outer abundance: 1e-9, V_{turb}=1.0kms^{-1}, no infall

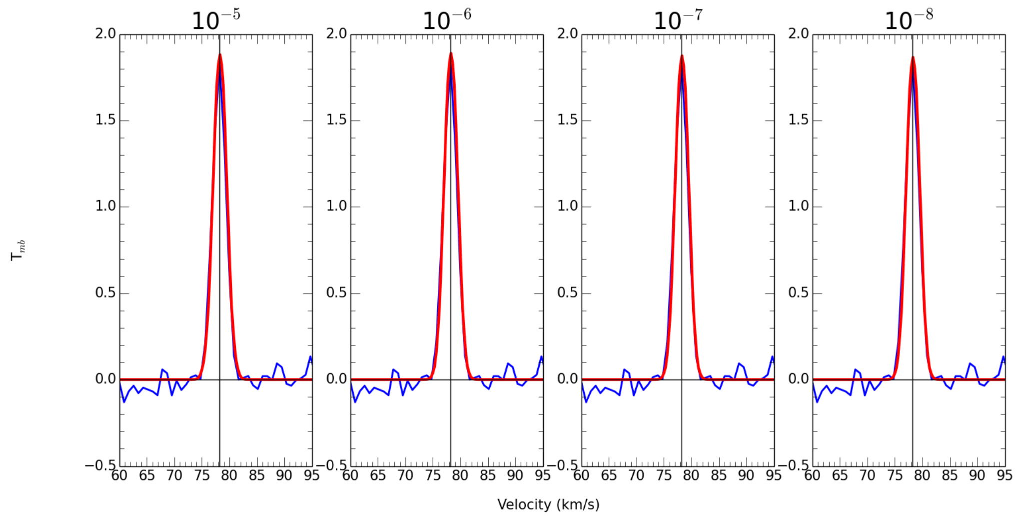

Figure 4.3: Outer abundance:1.9e-8,
V_{turb}:1.6km.s,
Infall:0.0kms^{-1}

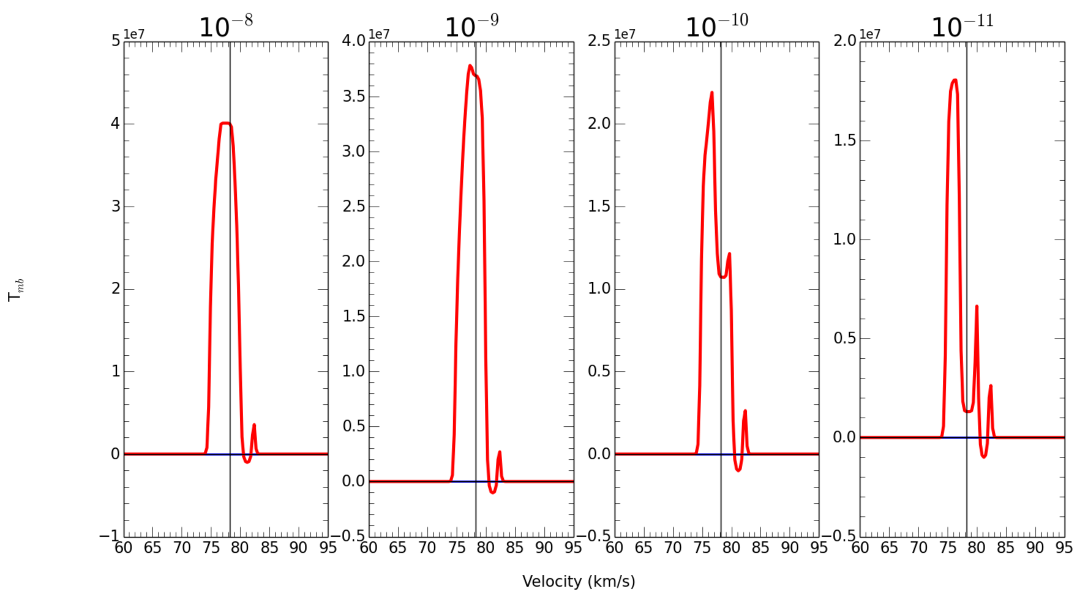

Figure 4.4: G28-MM N_2H^+ (6-5)model varying inner abundance with 0.00038" beamsize. Outer abundance: 1.6e-9, V_{turb}: 0.6kms^{-1}, Infall:2.7kms^{-1}

The beam size in Figure 4.4 was set to 0.00038", 10^5 times smaller than Herschel's beam size. Indeed, now we see that the inner abundance does show a significant change in the models with varying inner abundance. However, this beam size is still 100 times smaller than ALMA's 12km baseline (230GHz) beam size.

4.4 Issues with the N_2H^+ (3-2) Models

We've seen in Figures 3.9 and 3.15 that the N_2H^+ (3-2) lines for G28-MM and G11-MM show two turbulent components and a lack of accurate line shape, respectively. To examine this further, I investigated the N_2H^+ (1-0) map for G28-MM and G11-MM. Although the N_2H^+ (1-0) line is likely to probe a colder, more extended region that the (3-2)line, it will still offer insight into the spatial distribution of N_2H^+.

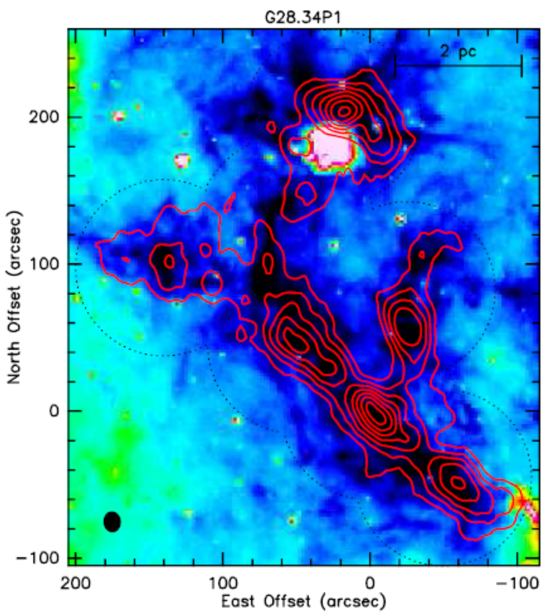

Figure 4.5: GLIMPSE image of IRDC G28.34+0.06 at 8μm with BIMA N_2H^+ (1-0) contours(Pillai, 2006)

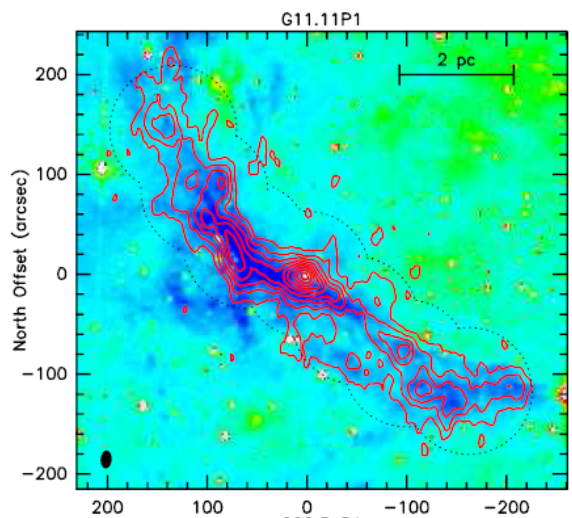

Figure 4.6: GLIMPSE image of IRDC G11.11-0.12 at 8μm with BIMA N_2H^+ (1-0) contours (Pillai, 2006)

In Figure 4.5 we can see that the emission from N_2H^+ (1-0) is quite extended. It is possible that the emission from the N_2H^+ (3-2) line may be more extended than RATRAN predicts, given the total radius of the temperature and density profile. The total angular size of the G28-MM temperature/density model corresponds to 21" (0.7pc or 1.5e5AU) and thus foreground (w.r.t the model) N_2H^+ (3-2) emission may be absent in the model. I propose that the extended wing (2kms^{-1} in Figure 3.9) emission is being formed at a further distance from the core than is modelled, leading to the two turbulent velocity components required to fit the peaks and the wings of the N_2H^+ (3-2) line in G28-MM. The model is consistent with the peaks of the line with 0.9kms^{-1} (Figure 3.9) as the peaks are emitted within the model radius.

Figure 4.6 shows the integrated intensity map of N_2H^+ (1-0) for G11.11-0.12. Again the emission of the N_2H^+ (1-0) should probe colder, more extended filamentary regions but it should give further indication of where the spatial distribution of N_2H^+ (3-2) emission lies.

As shown in the sections above, N_2H^+ (3-2) line for G11-MM appears to be the most difficult to model. The intensity and line shape is not consistent with a single model. The reason for this could be due to the emission coming from foreground N_2H^+. The total temperature/density model size for G11-MM corresponds to 16" (0.4pc or 8e4AU). As with G28-MM it is plausible that the model does not take all the N_2H^+ (3-2) emission from the filament into account, thus leading to inaccurate intensities and line shapes.

4.5 Kinematic Step Function

The kinematic step function shown in Figure 3.18 and Figure 3.13 produce consistent models for all the observed lines in both G28-MM and G11-MM. However, as we can see by the error bar in the kinematic parameters, it is not certain that the outer most step function is required as the errors in the N_2H^+ (3-2) and $C^{17}O$ (3-2) radius are greater than the size of the step function, making is statistically uncertain. However, the step from the N_2H^+ (6-5) radius and the outer radii are statistically significant, as the error are smaller than the size of this jump.

5 Conclusion

The dynamical structure of these cores are quite complex. The emission lines from N_2H^+ and $C^{17}O$ are shown to probe different radii from the sources. Theoretical infall velocities do not correlate very well with the observed line, leading to the assumption that more complex processes are taking place, which is not easily modelled using the techniques described above.

However, once a simpler kinematic step function model was implemented, the infall velocity was shown to increase towards the center of both G28-MM and G11-MM. The N_2H^+ (6-5)line probed a higher temperature region and shows a higher infall velocity than N_2H^+ 3-2, which probes the colder, outer envelope.

The kinematic structure found in this project agree with the general conclusions from other studies, that in high and low mass star formation the turbulent velocity increases outward from the centre and that the envelopes surrounding protostellar objects (high and low mass) show signs of infalling gas. This conclusion is supported by previous observations and studies mentioned above.

The G11-MM N_2H^+ (3-2)line emission is possibly more extended than the given temperature and density profiles allow to model. This may also be the case for the two turbulent components in the G28 N_2H^+ (3-2)line required to fit the observed line.

The abundance values found in this project are consistent with previous results of N_2H^+, $C^{17}O$.

The Chi-square was required in order to estimate the error ranges in each of the best fitting parameters.

References

R. Behrend and A. Maeder. Formation of massive stars by growing accretion rate. *A&A*, 373:190–198, July 2001. doi: 10.1051/0004-6361:20010585.

H. Beuther, E. B. Churchwell, C. F. McKee, and J. C. Tan. The Formation of Massive Stars. *Protostars and Planets V*, pages 165–180, 2007.

Philip R. Bevington and D. Keith Robinson. *Data Reduction and Error Analysis for the Physical Sciences*. McGraw-Hill Education, 2002.

S. J. Carey, F. O. Clark, M. P. Egan, S. D. Price, R. F. Shipman, and T. A. Kuchar. The Physical Properties of the Midcourse Space Experiment Galactic Infrared-dark Clouds. *ApJ*, 508:721–728, December 1998a. doi: 10.1086/306438.

S. J. Carey, F. O. Clark, M. P. Egan, S. D. Price, R. F. Shipman, and T. A. Kuchar. The Physical Properties of the Midcourse Space Experiment Galactic Infrared-dark Clouds. *ApJ*, 508:721–728, December 1998b. doi: 10.1086/306438.

Luis Chavarria. private communication, 2015.

H.-R. Chen, S.-Y. Liu, Y.-N. Su, and Q. Zhang. Deuterium Fractionation as an Evolutionary Probe in the Infrared Dark Cloud G28.34+0.06. *ApJ*, 713:L50–L54, April 2010. doi: 10.1088/2041-8205/713/1/L50.

M. P. Egan, R. F. Shipman, S. D. Price, S. J. Carey, F. O. Clark, and M. Cohen. A Population of Cold Cores in the Galactic Plane. *ApJ*, 494:L199–L202, February 1998.

S. Feng, H. Beuther, Q. Zhang, T. Henning, H. Linz, S. Ragan, and R. Smith. Are Infrared Dark Clouds Really Quiescent? *ArXiv e-prints*, March 2016.

Prof. Dale E. Gary. Radiative transfer. University Lecture, 2012.

T. T. Helfer and L. Blitz. Dense Gas in the Milky Way. *ApJ*, 478:233–245, March 1997.

F. Herpin, L. Chavarría, F. van der Tak, F. Wyrowski, E. F. van Dishoeck, T. Jacq, J. Braine, A. Baudry, S. Bontemps, and L. Kristensen. The massive protostar W43-MM1 as seen by Herschel-HIFI water spectra: high turbulence and accretion luminosity. *A&A*, 542:A76, June 2012. doi: 10.1051/0004-6361/201118413.

F. Herpin, L. Chavarría, T. Jacq, J. Braine, F. van der Tak, F. Wyrowski, E. F. van Dishoeck, A. Baudry, S. Bontemps, L. Kristensen, M. Schmalzl, and J. Mata. Herschel-HIFI view of mid-IR quiet massive protostellar objects. *A&A*, 587:A139, March 2016. doi: 10.1051/0004-6361/201527786.

M. R. Hogerheijde and F. F. S. van der Tak. An accelerated Monte Carlo method to solve two-dimensional radiative transfer and molecular excitation. With applications to axisymmetric models of star formation. *A&A*, 362:697–710, October 2000.

R. B. Larson. Turbulence and star formation in molecular clouds. *MNRAS*, 194: 809–826, March 1981. doi: 10.1093/mnras/194.4.809.

S. Leurini, C. Codella, A. López-Sepulcre, A. Gusdorf, T. Csengeri, and S. Anderl. SiO excitation from dense shocks in the earliest stages of massive star formation. *A&A*, 570:A49, October 2014. doi: 10.1051/0004-6361/201424251.

C. F. McKee and J. C. Tan. The Formation of Massive Stars from Turbulent Cores. *ApJ*, 585:850–871, March 2003. doi: 10.1086/346149.

O. Miettinen. A molecular line study of the filamentary infrared dark cloud G304.74+01.32. *A&A*, 540:A104, April 2012. doi: 10.1051/0004-6361/201118552.

O. Miettinen and S. S. R. Offner. Dynamics, CO depletion, and deuterium fractionation of the dense condensations within the fragmented prestellar core Orion B9-SMM 6. *A&A*, 555:A41, July 2013. doi: 10.1051/0004-6361/201321481.

L. Olmi, C. M. Persson, and C. Codella. Herschel-HIFI observations of H_2O, NH_3, and N_2H^+ toward high-mass starless and protostellar clumps identified by the Hi-GAL survey. *A&A*, 583:A125, November 2015. doi: 10.1051/0004-6361/201526901.

T. Pillai, F. Wyrowski, K. M. Menten, and E. Krügel. High mass star formation in the infrared dark cloud G11.11-0.12. *A&A*, 447:929–936, March 2006. doi: 10.1051/0004-6361:20042145.

Thushara Pillai. *The Initial Conditions of High Mass Star-Formation.* PhD thesis, Universitts und Landesbibliothek Bonn, 2006.

I. San José-García, J. C. Mottram, E. F. van Dishoeck, L. E. Kristensen, F. F. S. van der Tak, J. Braine, F. Herpin, D. Johnstone, T. A. van Kempen, and F. Wyrowski. Linking low- to high-mass young stellar objects with Herschel-HIFI observations of water. *A&A*, 585:A103, January 2016. doi: 10.1051/0004-6361/201525708.

F. L. Schöier, F. F. S. van der Tak, E. F. van Dishoeck, and J. H. Black. An atomic and molecular database for analysis of submillimetre line observations. *A&A*, 432: 369–379, March 2005. doi: 10.1051/0004-6361:20041729.

R. F. Shipman, F. F. S. van der Tak, F. Wyrowski, F. Herpin, and W. Frieswijk. The physical conditions in IRDC clumps from Herschel/HIFI observations of H_2O. *A&A*, 570:A51, October 2014. doi: 10.1051/0004-6361/201423912.

D. R. Soderblom, L. A. Hillenbrand, R. D. Jeffries, E. E. Mamajek, and T. Naylor. Ages of Young Stars. *Protostars and Planets VI*, pages 219–241, 2014.

Steven W. Stahler and Francesco. Palla. *The Formation of Stars.* WILEY-VCH Verlag GmbH & Co. KGaA,Weinheim, 2004.

Andrea Stolte. The formation of massive stars. University Lecture, 2013.

H. S. Thomas and G. A. Fuller. The circumstellar environment of high-mass protostellar objects. IV. $C^{17}O$ observations and depletion. *A&A*, 479:751–760, March 2008. doi: 10.1051/0004-6361:20066499.

M. H. D. van der Wiel and R. F. Shipman. Characterizing star formation activity in infrared dark cloud MSXDC G048.65-00.29. *A&A*, 490:655–664, November 2008. doi: 10.1051/0004-6361:200809696.

C. K. Walker, G. Narayanan, and A. P. Boss. Spectroscopic signatures of infall in young protostellar systems. *ApJ*, 431:767–782, August 1994. doi: 10.1086/174528.

Q. Zhang, Y. Wang, T. Pillai, and J. Rathborne. Fragmentation at the Earliest Phase of Massive Star Formation. *ApJ*, 696:268–273, May 2009. doi: 10.1088/0004-637X/696/1/268.

H. Zinnecker and H. W. Yorke. Toward Understanding Massive Star Formation. *ARAA*, 45:481–563, September 2007. doi: 10.1146/annurev.astro.44.051905.092549.

Appendices

Appendix A-RATRAN Parameters

- Temperature jump: Defines a radius where the boundary between the inner and outer abundance occurs given a certain temperature (typically 100K).
- Inner and outer abundance: Affects the intensity of the line by raising or lowering the abundances. Higher abundance, more emission.
- Turbulent Velocity: Width of the line can be varied. (NOTE: This is the σ of the line, ie FWHM = 2.354 * σ).
- Infall/Expansion velocity: Affects the shape of the line (blueshifted/redshifted), but also affects line intensity.
- Turbulent velocity exponent and Infall velocity exponent.
- Number of test photons: affects the time taken to run model and limits the randomness of the Monte Carlo Method.
- Telescope Beam size and Transition numbers
- V_{lsr}: Obtained from previous observations. (Shipman et al., 2014)

Appendix B - Infall exponent

$$V_{inf} = \left(\frac{GM}{R}\right)^{1/2} \tag{.1}$$

(Stahler and Palla, 2004)

where G is the gravitational constant, M is the source mass and R is the radius from the source.

RASM allows the user to add an exponent to the RATRAN parameters such as infall velocity. Once an initial infall velocity has been given (placed at the outer most radius of the model), RASM calculates how the velocity will increase or decrease with radius, depending on whether a positive or negative exponent is chosen. Taking an radial exponent of $R^{-0.5}$ for the infall velocity should be consistent with theoretical infall velocities (Eq. .1) for both lines at there respective radii (based on excitation temperature). A series of initial infall velocities were chosen and were set to increase inward with an $R^{-0.5}$ profile. This result is shown in Figure .1.

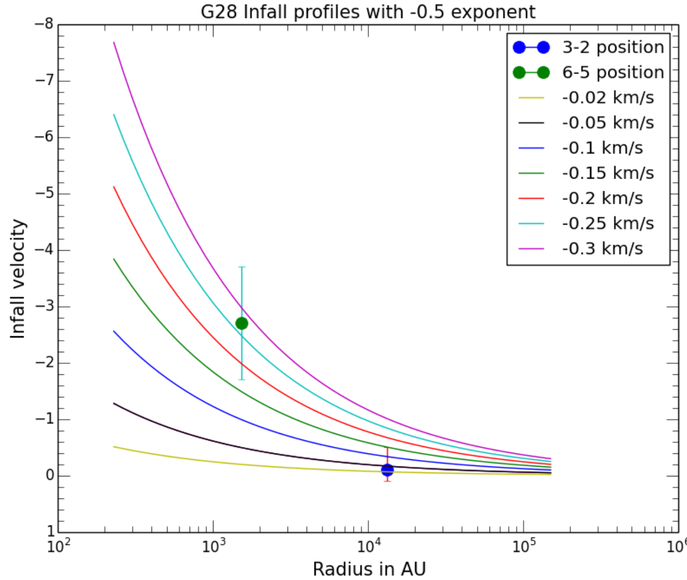

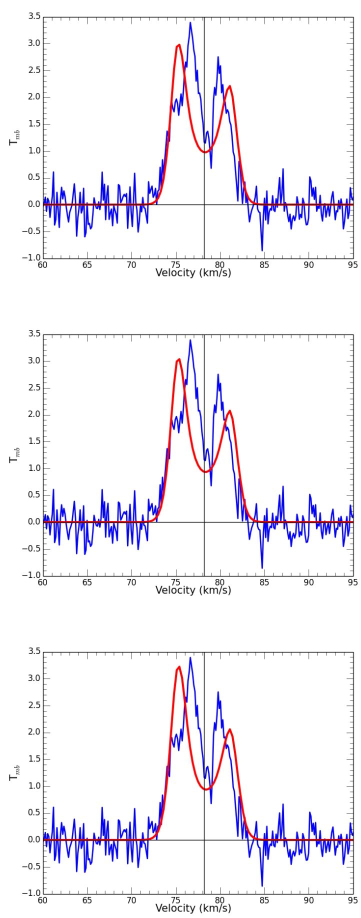

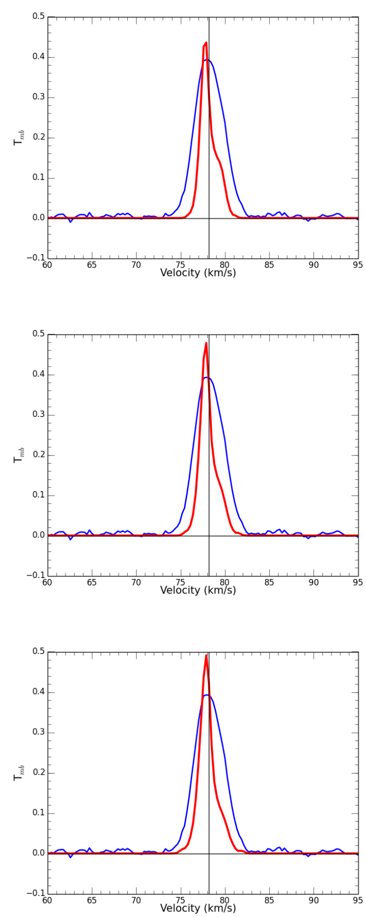

Figure .1: N_2H^+ (3-2) and (6-5) exponent models for -0.2, -0.25 and -0.3 staring positions. Exponent is set to -0.5.

We can see from the exponent models in Figure .1 that the models are inconsistent with the data, even though the errors in the infall velocity values are quite large and fall within numerous initial infall velocity profiles.

Acknowledgements

I would like to sincerely thank my Supervisor, Russ Shipman. Your support, advice, guidance and patience were greatly appreciated throughout my project. Our weekly discussions and brain-storming session really helped fuel my passion for this research. I thoroughly enjoyed working with you and learned so much from you along the way.

I would also like to extend thanks my co-supervisor Floris Van der Tak for his help and guidance throughout the course of my project.

Thanks also to Migo Muller, for acting as third reader of my thesis.

A special thanks to my Parents for their unending moral support and financial assistance throughout my study. I truly could not have done this without you.